Medicane Zorbas: Origin and impact of an uncertain potential vorticity streamer

Raphael Portmann[1], Juan Jesús González-Alemán[2], Michael Sprenger[1], and Heini Wernli[1]

[1]ETH Zurich, Institute for Atmospheric and Climate Science, Zurich, Switzerland
[2]University of Castilla-La Mancha, Environmental Sciences Institute, Toledo, Spain

Correspondence: Raphael Portmann (raphael.portmann@env.ethz.ch)

Abstract. Mediterranean tropical-like cyclones (Medicanes) can have high societal impact and their accurate forecast remains a challenge for numerical weather prediction models. They are often triggered by upper-level potential vorticity (PV) anomalies, such as PV streamers and cut-offs. But knowledge is incomplete about their detailed formation processes and factors limiting their predictability. This study exploits a European Centre for Medium-Range Weather Forecast (ECMWF) operational ensemble forecast with an uncertain PV streamer over the Mediterranean, which, three days after initialisation, resulted in an uncertain development of Medicane Zorbas in September 2018. Using an ad-hoc clustering of the ensemble members according to the PV streamer position, it is demonstrated that uncertainty in the initial conditions near an upper-level jet streak over the Gulf of Saint Lawrence is the dominant source of the subsequent uncertainty in the position of the PV streamer over the Mediterranean. The initial condition uncertainty strongly amplifies baroclinically after 18 h in a region of strong quasi-geostrophic forcing for ascent in the left exit of a jet streak over the North Atlantic. The further amplification and downstream propagation of the tropopause-level PV uncertainty leads to a large spread in the position of the PV streamer over the Mediterranean after three days, directly limiting the predictability of the position, thermal structure and evolution of Zorbas. Two low-level airstreams possibly play a key role in linking the uncertainties of the large-scale upper-level flow with meso-scale uncertainties in the cyclone structure. Overall, this study is an illustrative example that uncertainties in large-scale initial conditions can determine the practical predictability limits of a high-impact weather event.

1 Introduction

1.1 Medicanes: high impact, limited understanding, and uncertain forecasts

In the last 15 years, there has been increasing research on cyclones placed at the interface between the the classical concepts of tropical and extratropical cyclones. Several studies focused on so-called subtropical cyclones (STCs; e.g. Guishard et al., 2009; González-Alemán et al., 2015). STCs are low pressure systems that initially form from baroclinic processes, but they later acquire tropical characteristics due to convective processes, while fronts dissolve. In the second phase convection begins to build a low-level warm core and the environment becomes more barotropic. STCs have gained attention because they can have substantial impacts on society (Guishard et al., 2007), but also because they potentially convert into fully-tropical cyclones, a process called tropical transition (Davis and Bosart, 2004).

25 A similar phenomenon occurs over the Mediterranean Sea. So-called Medicanes (Mediterranean Hurricanes; Emanuel, 2005; Tous and Romero, 2013) or Mediterranean tropical-like cyclones (Miglietta et al., 2013) are (most often) hybrid systems, i.e. between extratropical and tropical cyclones, which occasionally undergo tropical transition. If the latter occurs, they can amplify through air-sea feedback (Emanuel, 1986) and acquire the typical appearance of a hurricane (Emanuel, 2005) with convective cloud bands wrapped around a cloud-free central eye and a typical size of their associated cloud clusters on the

30 order of 300 km in diameter. In this case, convection forms a robust warm core that reaches the upper troposphere and is associated with strong horizontal pressure gradients, wind, and rainfall. This results in high damage, although Medicanes rarely attain hurricane intensity.

Medicanes can form when positive upper-level potential vorticity (PV) anomalies (e.g. PV streamers and cut-offs that result from Rossby wave breaking) reach the Mediterranean Sea. These PV anomalies trigger extratropical cyclogenesis and if they

35 are accompanied by substantial deep convection they can further develop into a Medicane (Emanuel, 2005; Tous and Romero, 2013; Miglietta et al., 2013; Cavicchia et al., 2014). The relative role of positive upper-level PV anomalies and air-sea interaction for the intensification of Medicanes is currently debated, as well as the question to which degree they are dynamically similar to tropical cyclones (see e.g. Fita and Flaounas, 2018). There seems to be a high case-to-case variability (Miglietta and Rotunno, 2019), and, given their infrequent occurrence, the systematic study of Medicanes, their formation dynamics, and

40 sources of forecast uncertainty remains a challenge (Miglietta, 2019). In addition, in situations with the formation of Medicane, ensemble prediction systems often show a large spread even at short lead times (e.g. Di Muzio et al., 2019). This study investigates the uncertain three-day ensemble prediction of Medicane Zorbas in September 2018, with the aim of better understanding the effect of large-scale upper-level dynamics on the formation of a warm-core Mediterranean cyclone. Other studies have shown that a detailed analysis of ensemble forecasts, especially of different scenarios offered by a particular ensemble

45 prediction, can be highly rewarding for better understanding the involved dynamics and the practical predictability limits. For example, such scenarios have been used to identify key dynamical elements limiting the predictability of tropical cyclones (Torn et al., 2015; Pantillon et al., 2016; González-Alemán et al., 2018; Maier-Gerber et al., 2019) and atmospheric blocking (Quandt et al., 2017).

1.2 Origin and amplification of forecast uncertainties in Rossby waves

50 Besides uncertainties inherent to the forecast model (e.g. due to parametrisations), a major source of uncertainty in numerical weather forecasts is the limited accuracy of initial conditions. In fact, even slight uncertainties in initial conditions typically grow with increasing forecast lead time and potentially result in very different large-scale weather patterns a few days to a week after initialisation (e.g. Lorenz, 1969; Leutbecher and Palmer, 2008). However, forecast uncertainty does not grow homogeneously but depends on the flow itself. To quantify this flow-dependent growth of forecast uncertainty, operational ensemble

55 predictions are conducted since the early 1990s and have continuously improved since then (Bauer et al., 2015; Palmer, 2018). The uncertainty can be quantified with the ensemble spread that serves as a proxy for the expected forecast error of the ensemble mean if the forecast is reliable (which is not true in all flow situations, see Rodwell et al., 2018). Understanding forecast uncertainty and error is crucial to reveal the limits and potential for improving weather forecasting systems. In recent years,

...

research increasingly focused on the origin and amplification of forecast errors along the upper-level wave guide, i.e. the near-
tropopause band with a high isentropic PV gradient (Davies and Rossa, 1998; Schwierz et al., 2004) because there they tend to
amplify and propagate downstream due to Rossby wave dynamics (e.g. Dirren et al., 2003; Hakim, 2005; Davies and Didone,
2013). Such near-tropopause errors in Rossby waves can limit tropical cyclone predictability (e.g. Lamberson et al., 2016) and
they can also become relevant for Medicanes related to breaking Rossby waves that form strong upper-level PV anomalies over
the Mediterranean.

Many studies used the PV framework to investigate forecast errors along the Rossby wave guide (for example Fehlmann and
Davies, 1997; Dirren et al., 2003; Davies and Didone, 2013; Gray et al., 2014; Baumgart et al., 2018). They can *originate* from
errors in initial conditions and have shown to result in so called "forecast busts" over Europe, i.e. periods of anomalously low
predictability (Rodwell et al., 2013; Magnusson, 2017; Grams et al., 2018). Also, the misrepresentation of diabatic processes
in the forecast model can induce PV errors, as for example in warm conveyor belts (Gray et al., 2014; Martinez-Alvarado et al.,
2016). Warm conveyor belts affect the Rossby wave guide via their low-PV outflow in the upper troposphere. PV errors near
the tropopause, due to errors in initial conditions and/or model physics, translate into Rossby wave errors that then propagate
downstream.

To become relevant, forecast errors in Rossby waves must *amplify*. Different case studies have shown that this can be due to a
range of processes. Baumgart et al. (2018) point out the importance of non-linear (barotropic) dynamics near the tropopause
and to a lesser extent baroclinic interaction and effects of upper-tropospheric divergent winds. The contribution of non-linear
tropopause dynamics to amplification (and downstream propagation) of forecast errors can be understood by the mutual inter-
action of negative and positive PV errors near the tropopause (Davies and Didone, 2013). Grams et al. (2018) identified warm
conveyor belts in a forecast bust case as key for amplifying forecast errors in the tropopause region. This process includes error
amplification in the baroclinic growth of a cyclone, possibly enhanced by model error in the representation of diabatic pro-
cesses in the warm conveyor belt, resulting in errors in the divergent wind and size and amplitude of the negative PV anomaly
in the upper troposphere. Together, these studies indicate that forecast errors in near-tropopause Rossby waves can grow just
due to their internal non-linear dynamics, but baroclinic coupling can, via rapid baroclinic growth or warm conveyor belts and
their associated low-PV outflow, enhance this amplification.

The relevance of these processes to the amplification of forecast errors and uncertainty is likely very case dependent and their
interplay potentially complex. However, only few case studies exist that investigate the origin, amplification and propagation
of forecast errors in Rossby waves and their impact on the uncertainty in the prediction of high-impact weather events.

1.3 Zorbas: An uncertain Medicane

In this context, we exploit the recent Medicane Zorbas, which rapidly acquired fully tropical-like characteristics. Operational
ensemble forecasts by the European Centre for Medium Range Weather Forecast (ECWMF) did not agree on the development
of Zorbas, even at short lead times. Zorbas, from the moment of its formation until it acquired full tropical-like characteristics,
led to considerable damage through severe winds, torrential rainfall, major flooding and even tornadoes. The main affected
region was Southern Greece, especially Crete, Peloponnese, Evia, and the region around Athens.

We investigate the origin and amplification of the forecast uncertainty associated with the PV streamer that triggered Zorbas (see Section 3) and identify the relevant large-scale conditions limiting the Medicane's predictability. The key questions of our study are: What is the origin of the forecast uncertainty in the PV streamer and which sequence of dynamical processes lead to its amplification and propagation into the Mediterranean? Was the uncertainty in the PV streamer the direct cause of the uncertain Medicane prediction and why? This study does not aim to analyze the details of the Medicane dynamics but rather focuses on the large-scale processes prior to the Medicane formation.

The remainder of this article is structured as follows. After describing the data used in this study we give an overview on the synoptic evolution of Zorbas and introduce the main method that builds the basis for all subsequent analyses. Then, the next Sections are organized as a journey from the origin of the large-scale forecast uncertainty to its effect on the uncertainty of the cyclone development and precipitation impacts. This is then connected to uncertainties in the low-level moisture and warm-air advection prior to the Medicane formation. Finally, uncertainties in the evolution of the vertical thermal structure of Zorbas are diagnosed and links to the relevant precursors discussed. We close with highlighting the main conclusions and discuss implications for further research on Medicane dynamics and on uncertainty in Rossby wave forecasts.

2 Operational ECMWF products

The basic data for this study is from the ECMWF Integrated Forecasting System (IFS, Cycle 45r1; ECMWF, 2018). We use the operational ensemble forecasts with 50 perturbed members initialized at 0000 UTC 24 Sep and 0000 UTC 27 Sep 2018 (46 perturbed members available), the operational analysis, and operational short-term forecast of 6-hourly accumulated precipitation, are used. The spectral resolution of the operational ensemble is TCO639 (about 18 km) on 91 model levels, and the resolution of the operational analysis TCO1279 (about 9 km) on 137 model levels. The data is available every 6 h and has been interpolated to a regular grid with a horizontal resolution of $1° \times 1°$. From the standard variables we additionally compute PV, equivalent potential temperature and quasi-geostrophic omega (QG ω) on 850 hPa as forced by levels above 550 hPa [computed the same way as in Graf et al. (2017)]. As a measure for forecast skill, anomaly correlation coefficients (ACC) are calculated for geopotential height at 500 hPa for each ensemble member of the forecasts initialized at 0000 UTC 24 Sep and 0000 UTC 27 Sep 2018.

3 Synoptic overview

Figures 1, 2 and 3 provide an overview of the atmospheric processes before and during the formation of Zorbas based on ECMWF operational analysis and infrared images from the European Organisation for the Exploitation of Meteorological Satellites (EUMETSAT). At 0000 UTC 26 Sep 2018, about a day before cyclogenesis, a few convective clouds (white patches) and some precipitation (red contours) can be identified in the Southern Mediterranean and Lybia (Fig. 1a). Convective activity is confirmed by the occurrence of lightning in this region (as inferred from www.lightningmaps.org, not shown). At this time, a large-scale trough is present over Eastern Europe (Fig. 2a). In the Mediterranean region, the low-level air masses (850 hPa)

have very high equivalent potential temperatures whereas in Eastern Europe the values are much lower (Fig. 3a) indicating
125   substantial baroclinicity and moisture gradients between these two regions.

In the evening of the same day, at 1800 UTC 26 Sep 2018, cloud formation and precipitation over the Mediterranean is enhanced (Fig. 1b). The upper-level trough has elongated into a narrow PV streamer on 325 K that extends towards the Central Mediterranean (Fig. 2b). At the streamer's downstream side (to the east), a large area of enhanced QG forcing for ascent by the upper levels (QG ω, red contour in Fig. 2b) provides favorable conditions for the relatively strong convective precipitation off
130   the Lybian coast [local maximum of $24\,\mathrm{mm}\,(6\,\mathrm{h})^{-1}$ indicated by the blue contours in Fig. 1b]. High wind speeds on 850 hPa over the Aegean Sea (arrows in Fig. 3b) indicate strong low-level cold air advection from Eastern Europe and the Black Sea region towards Greece and the Central Mediterranean. Cold and dry air masses that are advected over a warm ocean surface can enhance sea-surface latent heat fluxes and become relevant for Medicane formation (Miglietta and Rotunno, 2019).

A day later, at 1800 UTC 27 Sep 2018, the clouds have formed a spiral-like structure with a weak frontal cloud band extending
135   from the Mediterranean over Lybia (Fig. 1c). Surface cyclogenesis has taken place off the Lybian coast close to Benghazi (closed yellow contours in Fig. 3c) and increased gradients of equivalent potential temperature at this location (Fig. 3c) confirm the presence of a weak surface cold front. The PV streamer has broken up into segments (Appenzeller and Davies, 1992). Its tip has formed a C-shaped PV cut-off (shading in Fig. 2). To the east of it, a large region of enhanced QG ω (red contours) is present and strongly ascending air masses (black crosses, ascent rate larger than 600 hPa in 24 h) as identified from trajectory
140   calculations using the Lagrangian analysis tool LAGRANTO (Wernli and Davies, 1997; Sprenger and Wernli, 2015) are located in the dent of the cut-off, above the cyclone centre. This is where also the precipitation maximum occurs [$88\,\mathrm{mm}\,(6\,\mathrm{h})^{-1}$, red contours in Fig.1c]. The presence of rapidly ascending and strongly precipitating air masses are indicative for substantial diabatic effects [cf. the concept of warm conveyor belts; Joos and Wernli (2012); Binder et al. (2016)]. They not only heat the cyclone centre and potentially form a low-level positive PV anomaly but favor the direct erosion of the PV cut-off due to
145   diabatic PV modification and entrainment (Portmann et al., 2018). Furthermore, they transport low-PV air to the 325 K level, which causes the dent structure in the upper-level PV and further affects the evolution of the cut-off. The ascent seems to be strongly convective, as confirmed by the high lightning activity in this region (as inferred from www.lightningmaps.org, not shown).

At 1800 UTC 28 Sep 2018, almost no strongly ascending air masses are present on 325 K, the PV cut-off has almost completely
150   decayed on 325 K, and the enhanced QG ω has vanished (Fig. 2d). The surface cyclone has further intensified and moved over the Central Mediterranean. The satellite data shows a cyclone without clear frontal cloud bands and still substantial precipitation in its centre (Fig. 1d), which is, however, not associated with strong QG ω but likely due to conditional instability. The region with enhanced gradients of equivalent potential temperature previously identified as a weak cold front has moved eastward and become disconnected from the cyclone centre. A local maximum of low-level equivalent potential temperature is present
155   in the cyclone centre, indicating the formation of a warm seclusion (Shapiro and Keyser, 1990). Warm seclusion events have been previously linked to Medicane formation (Mazza et al., 2017). All this suggests that the cyclone underwent the transition from an extratropical to a subtropical-like or even tropical-like system between 1800 UTC 27 Sep and 1800 UTC 28 Sep 2018. As diagnosed from the cyclone phase space [CPS; Hart (2003), for more details see Sect.6.3], a low-level warm core is

already present at 1800 UTC 27 Sep and a deep warm core is reached only 12 hours later at 0600 UTC 28 Sep (see Fig 4a).

160 Consequently, Zorbas also visually acquires tropical characteristics including the formation of an eye on 29 September 2018 as it moves over Greece (not shown). However, this later period of the cyclone evolution is not in the focus of this study.

In summary, Zorbas forms via extratropical cyclogenesis forced by a breaking-up PV streamer over a baroclinic zone in the Central Mediterranean. As low-level moisture and temperature over the Mediterranean are very high and north-easterly cold air advection at low levels occurs, cyclogenesis is accompanied by strong convection, cloud formation and intense precipitation,

165 first at the PV streamers downstream flank and later in the cyclone centre. Zorbas then transitions into a subtropical and later even tropical-like system: It loses its frontal structures and becomes a circular cyclone with a warm seclusion, which is where most precipitation occurs.

4 Ensemble clustering according to position of PV streamer

The position of the PV streamer at 0000 UTC 27 Sep (shown in Fig. 2 six hours earlier) varies strongly in the ensemble forecast

170 initialized at 0000 UTC 24 Sep 2018, with about equal shares of ensemble members where the PV streamer is roughly correct, too far west and too far east, respectively. This offers the opportunity to use this ensemble forecast to study the dynamical processes that lead to this significant forecast uncertainty in the upper troposphere, which subsequently affected Medicane formation (see Sect.6). Therefore a pragmatic clustering method was designed to separate the strongly diverging PV streamer evolutions in these ensemble members into clusters with a similar evolution. The three identified PV streamer scenarios, i.e.

175 clusters, are the basis for all remaining analyses. For the clustering, a box is defined around the PV streamer as identified at 0000 UTC 27 Sep 2018 in the operational analysis (Mediterranean box, 5-30°E, 30-45°N, see black box in Fig. 4). The clustering uses PV vertically averaged from 320 to 330 K, where all tropospheric PV values (<2 PVU) are set to zero, hereafter called PV_{av}. Hence, PV_{av} is high in areas where the PV streamer is strong and deep, and low where it is weak and shallow. The clustering is based on two different steps: First, all ensemble members are identified for which the region with $PV_{av} \geq 2$ PVU

180 has more than 75% overlap with the corresponding area in the analysis. In these 19 members (cluster 1), the streamer has a similar shape and location as in the analysis (see blue shading in Fig. 4). The remaining members are separated into two clusters depending on whether the maximum PV_{av} is shifted to the west (cluster 2, 12 members, green shading in Fig. 4) or east (cluster 3, 18 members, green shading in Fig. 4) relative to the analysis. There is one ensemble member that can not be attributed to one of the three clusters because its overlap is less than 75% and the maximum of PV_{av} is located at the same

185 longitude as in the analysis.

The meaningfulness of this clustering for understanding predictability is supported by the fact that it helps explaining the temporal development of the ACC in the Mediterranean box. To this aim, Fig. 5a summarizes the synoptic sequence of the case, i.e. the formation of the PV streamer over the Mediterranean, the break-up resulting in a PV cut-off (grey boxes), the minimum sea-level pressure of Zorbas (solid line) and its thermal structure as diagnosed from the CPS (colors, for details see

190 Sect.6.3). As shown in Fig. 5b, the ACC of geopotential height at 500 hPa in the Mediterranean starts to drop (median and many members in clusters 2 and 3), when the PV streamer reaches the Mediterranean on 26 Sep 2018 and cyclogenesis occurs,

while it remains high (close to 1) until 29 Sep 2018 for most members of cluster 1 (blue lines in Fig. 5b). After the drop from 1 to around 0.8 the median ACC remains fairly constant until 29 Sep 2018. In comparison, for the ensemble forecast initialized at 0000 UTC 27 Sep 2018, i.e. at the time when the PV streamer has developed, the ACC remains high in all members during

195   the intensification and deepest phase of Zorbas, dropping only after 29 Sep 2018 (Fig. 5c), likely due to errors associated with a second streamer reaching the Mediterranean in the northern part of the box (not shown).

We conclude that errors in the position and shape of the PV streamer limited the large-scale predictability as measured by the ACC of geopotential height on 500 hPa in the Mediterranean, and that the clustering incorporates the relevant characteristics of the PV streamer well. However, the ACC of geopotential height on 500 hPa does not fully account for errors in the vertical

200   structure of the cyclone and its intensity and exact position, aspects that are potentially relevant for predicting the cyclone's impact. Hence, even if the large-scale predictability related to the PV streamer is high, still there can be relevant errors in the details of the cyclone evolution and its interaction with the upper levels, which may severly limit meso-scale predictability.

5   PV streamer scenarios emerge from initial condition uncertainties and baroclinic amplification

We now investigate how the diverging PV streamer scenarios identified in Sect.4 emerge from differences in initial conditions

205   that amplify baroclinically at the left exit of a jet streak over the North Atlantic. To this end, we analyze the differences of the means of clusters 2 and 3 as these are the clusters that deviate the most in terms of the PV streamer evolution. We investigate the upper-level development using differences in PV and winds on 325 K (Fig. 7a-d), and the baroclinic interaction with the lower levels using QG ω and geopotential height on 850 hPa (Fig. 7e-h). For upper-level PV and winds, we use normalized cluster-mean differences (Torn et al., 2015):

210    $$\Delta PV = \frac{\overline{PV_3} - \overline{PV_2}}{\sigma_{PV}} \tag{1}$$

where σ_{PV} is the standard deviation of all ensemble members. Hence, ΔPV becomes large when the cluster-mean difference of PV at a given location is much larger than the ensemble standard deviation at the same location, i.e. when the two clusters contain the members of the ensemble that are most different from each other. Large absolute differences in regions of strong gradients, particularly at the tropopause, are given less weight. Additionally, it allows us to easily compare different lead

215   times. For example, if ΔPV increases with lead time, the cluster differences grow faster than the ensemble standard deviation, which means that the clusters become increasingly distinct from each other, relative to the full ensemble. Further, in order to make statistically robust statements, regions where cluster-mean PV values significantly differ are identified using a two-sided Wilcoxon rank-sum test (see supplementary material). By design, significant PV differences tend to be co-located with high values of ΔPV.

220   Already at 0000 UTC 24 Sep 2018, i.e. the initialization time of the forecast, a relatively large area of significantly positive PV differences is discernible on the stratospheric side of a jet streak over the Gulf of Saint Lawrence (teal contour in Fig. 6). The normalized PV differences in this area are between 0.5 and 1.5 standard deviations (red shading in Fig. 6). With increasing lead time this PV difference in the initial conditions moves eastward along the 2-PVU contour, amplifies over the North Atlantic

and produces a dipole of negative and positive PV differences further downstream that ultimately result in the differences in

225 the PV streamer formation over the Mediterranean (Figs. 7a-d). In the following, this development is discussed in more detail. The initial PV difference as shown in Fig. 6 moves eastward and after 6 h is located northeast of Newfoundland, with an amplitude still between 0.5 to 1.5 standard deviations (Fig. 7a). After 18 h (Fig. 7b), the PV difference is largest over the central North Atlantic, has amplified, reaching values above 1.5 standard deviations, and covers a larger area. Also, the mean 2-PVU contours of clusters 2 (dashed) and 3 (solid) start to separate at this location and a clear cyclonic difference wind field (arrows)

230 is present. Additionally, downstream of the positive PV difference, a negative PV difference north of the British Isles emerges. In the following 24 h (Figs. 7c,d) both PV differences propagate along the wave guide and the maximum amplitude propagates from the positive to the negative PV difference. Another positive PV difference occurs further downstream (red patch at 43°N and between 20°E and 30°E in Fig. 7d). This gradual downstream development of the original PV difference can be explained by non-linear (barotropic) Rossby wave dynamics: The cyclonic difference wind field leads to stronger northward advection of

235 tropospheric low-PV air in cluster 3 compared to cluster 2 downstream of the positive PV difference, leading to a negative PV difference there. This negative PV difference then propagates downstream and induces a positive PV difference by the same mechanism. At 1800 UTC 25 Sep 2018, the 2-PVU contours are clearly separated, showing a westward phase shift and larger amplitude of the Rossby wave in cluster 2 (dashed contour) compared to cluster 3 (solid contour). Hence, this amplification and downstream development of the PV differences result in the diverging formation of the PV streamer, which forms earlier

240 and more to the west in cluster 2 and later and more to the east in cluster 3 (consistent with Fig. 4).

Figures 7e-h show how the diverging upper-level wave propagation interacts with the lower troposphere. Upper-level PV differences project to the surface via QG ω (shown in red contours in Figs. 7e-h). Six hours after initialization (Fig. 7e), cluster-averaged geopotential height (purple contours) and potential temperature (not shown) on 850 hPa are still almost identical. The regions of upper-level induced QG ω on 850 hPa (red contours) have slightly different magnitudes but are well aligned. As the

245 upper-level PV differences intensify, QG ω becomes stronger in that region (red contours with a maximum around 58°N and 35°W in Fig. 7f), which is associated to the left exit of an upper-level jet streak (blue and green shading). The jet streak and the resulting forcing for ascent in cluster 2 (green shading and dashed contours) are slightly shifted to the northwest compared to cluster 3 (blue shading and solid contours). These differences are partially significant (see supplementary material). In the region of the forcing, a wave-like stucture in geopotential height (purple contours) and potential temperature (not shown)

250 occurs, indicating the initiation of a baroclinic wave. QG ω and the baroclinic wave propagate further in both clusters, but in cluster 2 the center of action is more to the west (Figs. 7g,h). At 0600 UTC 25 Sep 2018 (Fig. 7h), closed contours in geopotential height indicate the presence of a cyclone in both clusters, and the shifts in all fields between clusters 2 and 3 become more evident.

To sum up, the uncertainty of the position of the Mediterranean PV streamer can be traced back to initial condition uncertainty

255 on the poleward side of an upper-level jet streak over the Gulf of Saint Lawrence. This uncertainty amplifies as it moves into the left-exit region of a jet streak over a strongly baroclinic zone 18 h after the forecast is initialised. Via the strong QG forcing for ascent in this cyclogenetic region the upper-level uncertainties couple with the lower level, grow, and give rise to an uncertain low-level wave in a baroclinic zone. Hence, most likely, the upper-level uncertainties amplify due to the exponential growth

inherent to baroclinic instability. However, after this about 12-18 h lasting period of strong vertical coupling and co-location of
260   upper- and lower-level uncertainties, the amplified upper-level uncertainties propagate via non-linear Rossby wave dispersion
faster downstream than the low-level wave. They reach the Mediterranean region while the low-pressure system resulting from
this interaction becomes stationary east of Iceland.

6   Diverging synoptic development impacts Medicane predictability

Having elucidated the reason for the uncertainty in the position of the PV streamer, we now have a closer look at how this
265   uncertainty affects the subsequent cyclone development in the Mediterranean. In addition, we analyze how the PV streamer
scenarios affect the potential precursors for the formation of a low-level warm core, which is crucial for the meso-scale dynam-
ics of the transition of an extratropical to a Medicane-like cyclone. Finally, we diagnose the predicted number of Medicane-like
systems in each cluster and discuss the relevant large-scale precursors.

6.1   Synoptic development over the Mediterranean

270   To examine the diverging synoptic development we analyze for all three clusters the evolution of mean upper-level PV as well
as geopotential height on 850 hPa and surface precipitation. Regions where these fields significantly differ between two clusters
are identified using a two-sided Wilcoxon rank-sum test (see supplementary material). Figure 8 shows the three upper-level PV
streamer scenarios from clusters 1-3 and how they translate into distinct low-level cyclogenesis scenarios.

Before the formation of the narrow PV streamer, at 1200 UTC 25 Sep 2018, i.e. 36 hours after forecast initialisation (Figs.
275   8a,e,i), the differences between the three clusters are significant in the region between 8-15°E and 48-55°N (indicated by the
teal patches in Figs. 8e,i). These differences are exactly the ones investigated in the previous Sect.(compare Figs 7c,d). While
the 2-PVU contour of cluster 1 is very similar to the analysis, the contour is clearly shifted to the west compared to the analysis
in cluster 2 and to the east in cluster 3. At 1200 UTC 26 Sep 2018, after the narrow PV streamer has formed, the differences
between the clusters become more obvious (Figs. 8b,f,j). The shape and position of the streamer in cluster 1 is still very close to
280   the analysis, whereas in cluster 2 the tip of the streamer is thinner and extends more to the west, and in cluster 3 it is shifted to
the east. In these regions, clusters 2 and 3 significantly differ from cluster 1 (see supplementary material). This is not surprising
as the clustering was specifically designed to focus on these differences.

After the PV cut-off formation, at 1200 UTC 27 Sep 2018 (Figs. 8c,g,k) the differences in the scenarios over the Mediterranean
are very prominent. While in cluster 1, the cut-off is located south of Italy in the Central Mediterranean (as in the analysis),
285   cluster 2 exhibits a much weaker cut-off shifted to the west over Tunisia and cluster 3 a stronger cut-off shifted to the east
over the Eastern Mediterranean. In all clusters surface cyclogenesis occurs slightly east of the cut-off (closed purple contours
and black circles), which is where we expect the strongest QG forcing for ascent (as visible in Fig. 2). Hence, in cluster 1 the
cyclone forms in northeastern Lybia (as in the analysis, indicated by the teal star), in cluster 2 in northwestern Lybia close to
Tripoli, and in cluster 3 in the Eastern Mediterranean over Crete. At this stage, cluster 3 exhibits the strongest, most developed
290   surface cyclone.

One day later, at 1200 UTC 28 Sep 2018 (Figs. 8d,h,l), the cut-off in the analysis has decayed already into smaller patches due to the effects of strong latent heat release in rapidly ascending and precipitating air masses, as discussed in Sect.3. In cluster 1 the cut-off has clearly weakened (PV values < 3 PVU), in cluster 2 it fully decayed, and in cluster 3 it is still very prominent and strong (PV values > 6 PVU), indicating substantial differences in latent heat release. In both clusters 1 and 3 the vertical structure of the system has become more barotropic, i.e. the cut-off and the surface cyclone are vertically aligned. In cluster 1 the cyclone has further intensified with the minimum cluster-mean sea-level pressure dropping from 1010 hPa to 1007 hPa (not shown), whereas in clusters 2 and 3 it has weakened from 1011 hPa to 1013 hPa and from 1009 hPa to 1011 hPa, respectively. The accumulated cluster-mean precipitation during the period when most members exhibit a cyclone track (1800 UTC 26 Sep - 0000 UTC 30 Sep 2018) clearly differs between the three clusters (shading in Fig. 9a-c; differences are statistically significant, see supplementary material). In all clusters the precipitation mainly occurs in the immediate surrounding of the cyclone tracks (red lines), with maximum values in the Central Mediterranean near 20°W and about 500 km further southwest and northeast in clusters 2 and 3, respectively. This, of course, is consistent with the positions of the PV streamer and cut-off. Cluster 3 is associated with the smallest precipitation area, whereas the areas of clusters 1 and 2 are of similar size. The precipitation pattern in cluster 1 matches best with the short-term forecast, but the precipitation amounts are smaller, also due to the smoothing effect from averaging. The cyclone tracks in cluster 1 also fit best the observed track in the first half of the life cycle. However, there is no cyclone track in the ensemble that closely follows the observed one in the second part of the life cycle, when the cyclone moves over Greece and leads to substantial precipitation over the Peleponnes, the Athens region, and Evia.

We conclude that the uncertainties in the PV streamer's zonal position over the Mediterranean, as a consequence of the processes discussed in Sect.5, directly lead to uncertainties in the location of cyclogenesis and the amount and location of precipitation. For cluster 1, where the PV streamer location most closely matches with the analysis, the predicted cyclogenesis, cyclone tracks, PV cut-off evolution, and precipitation patterns also compare most favourable with the operational analysis and short-term forecasts. The uncertainty in the evolution of the PV cut-off likely directly affects the development of the cyclone and might be a crucial factor determining if a Medicane finally forms or not: If the cut-off is weak and decays early (as in cluster 2), the cyclonic circulation, destabilization, and quasi-geostrophic forcing for ascent are also weak and might not be sufficient to produce a strong cyclone with a deep warm core. We will elaborate further on this hypothesis in Sect.6.3.

6.2 Low-level airstreams relevant for Medicane formation

To investigate potential precursors of a low-level warm core and subsequent development of a Medicane-like system, we now focus on two different low-level air masses in the cyclone around cyclogenesis time: The air directly located in the cyclone centre and the air with the highest equivalent potential temperature in the warm sector of the cyclone, which could potentially be advected into the cyclone centre to form a warm seclusion. Note that we do not identify low-level warm cores directly and do not investigate their formation in detail. However, we hint on two airstreams that are potential precursors of a low-level warm core and are dominated by the large-scale situation in each cluster. We highlight the important differences between the clusters and use them to hypothesize about the relevance of the large-scale situation for the probability of transition into Medicane-like systems in each cluster. This probability is then quantified in the subsequent section.

325 For each ensemble member, 48-hour backward trajectories are calculated using the Lagrangian analysis tool LAGRANTO (Wernli and Davies, 1997; Sprenger and Wernli, 2015) (i) from all grid points on 850 hPa within a radius of 200 km around the cyclone centre, and (ii) from the 15% of grid points with the highest equivalent potential temperature within 500 km from the cyclone centre. With the latter, we aim to select the warmest and moistest air parcels in the warm sector of the developing cyclone. The backward trajectories are started at 1200 UTC 27 Sep 2018, which is at cyclogenesis in the operational analysis

330 and at or shortly after cyclogenesis in most ensemble members and, hence, before cyclone dynamics starts to dominate air mass advection. It is also before a warm core forms in the operational analysis and some ensemble members. Therefore, this timing allows identifying the large-scale airstreams prior to cyclogenesis and discussing their potential role as "predictors" for the development of a Medicane-like cyclone.

Figure 10 shows, for each ensemble member and separate for the three clusters, the 48-hour backward trajectories averaged for

335 all selected grid points (coloured lines). For each cluster, shading indicates the distribution of the air parcels at 1200 UTC 27 Sep 2018 (red) and 48 h before (purple). The air parcels in the cyclone centre (Fig. 10a-c) originate mainly from the western part of the Black Sea and Eastern Europe in all three clusters (see purple shading and coloured diamonds). On the contrary, the air parcels with the highest equivalent potential temperature in the warm sector of the cyclone (Fig. 10d-f) originate from the Central Mediterranean in clusters 1 and 2 but from the Black Sea in cluster 3.

340 The evolution of equivalent potential temperature (Fig. 11a-c), potential temperature (Fig. 11d-f) and specific humidity (Fig. 11g-i) along the backward trajectories reveals additional differences between cluster 3 and clusters 1 and 2. In cluster 3, the air parcels in the cyclone centre (blue shading) have an average equivalent potential temperature more than 7 K lower than in clusters 1 and 2, even though 48 h before the equivalent potential temperature was very similar in all clusters. To a large part, this can be attributed to a stronger increase in specific humidity (Fig. 11g-i) especially in the period between -36 h and -12 h.

345 The air parcels are, in contrast to cluster 3, transported over the Mediterranean (Fig. 10a-c) where they most likely moisten due to ocean evaporation. In the same period, potential temperature also increases more strongly in clusters 1 and 2, likely due to surface sensible heat fluxes. The rapid increase in potential temperature and drop in specific humidity in clusters 1 and 2 during the last 6 h clearly indicates strong latent heating due to cloud formation. This signal is almost entirely missing in cluster 3.

The air parcels selected in the warm sector of the cyclone have very different properties in clusters 1 and 2 compared to clus-

350 ter 3 already at their origin, when they are much moister and warmer (green shading in Fig. 11). However, they experience only a slight warming and moistening as they are transported into the warm sector, whereas in cluster 3 they are significantly moistened and heated. Nevertheless, the air parcels in cluster 3 are eventually still cooler and drier. In cluster 3, the temporal evolution of all three variables (Fig. 11c,f,i) is very similar for the air parcels selected in the cyclone centre (blue) and the ones in the warm sector (green), with the main difference that the latter are warmer and moister. In clusters 1 and 2, however, the air

355 parcels are part of airstreams with clearly distinct properties.

We conclude that in the ensemble members of clusters 1 and 2, the air which originates from the Black Sea / Eastern Europe region and later constitutes the cyclone centre substantially moistens as it is transported rapidly over the Central Mediterranean (wind speeds over the Bosporus reach above $20\,\mathrm{m\,s^{-1}}$ in the operational analysis, see Fig. 3). Previous studies have already pointed out the importance of strong surface fluxes for Medicane formation due to dry and cold winds reaching the

360   Mediterranean (Miglietta and Rotunno, 2019). Together with the destabilization and quasi-geostrophic forcing for ascent by the upper-level PV streamer/cut-off, this favours the strong latent heating of the air masses eventually constituting the cyclone centre. In cluster 3, this process is lacking as the cyclone formation occurs in the northern part of the Mediterranean. Hence, in clusters 1 and 2, moister and warmer air is present in the cyclone centre that could favour the transition into a Medicane-like cyclone. Moreover, the PV streamer is located such that very warm and moist air from the Central Mediterranean is advected

365   cyclonically into the warm sector, which might support the formation of a warm seclusion and transition into a Medicane-like cyclone. Again, in cluster 3 this process is lacking. Hence, from the perspective of low-level processes, clusters 1 and 2 favour the formation of a low-level warm core, whereas this is not the case for cluster 3. As caveat, we mention that this analysis neglects that the cyclone formation does not occur exactly at the same time in all members, and the stage of the cyclone may be slightly different in different members. Nevertheless, it provides a basic understanding of the fundamental differences in the

370   low-level processes between the clusters.

6.3   Explaining Medicane predictability

So far, the uncertain forecast of the PV streamer was shown to be directly linked to uncertainties in the position and magnitude of the PV cut-off, and the location of cyclogenesis and precipitation. Further, the eastward displacement of the PV streamer in cluster 3 leads to substantial differences in the low-level flow and, likely, air-sea interaction, compared to clusters 1 and 2.

375   We now argue that this helps to explain major differences in the vertical thermal structure of the cyclone in the three clusters and the extent to which it acquires tropical-like characteristics. To this aim, we consider the cyclone phase space (CPS; Hart, 2003), which is a useful tool to diagnose the thermal structure of cyclones.

Cyclone tracks at 6-h temporal resolution are obtained for each of the 50 ECMWF ensemble members and the operational analysis using the cyclone detection and tracking method described by Picornell et al. (2001). This method was specifically de-

380   signed to study meso-scale cyclones in the Mediterranean Sea, including Medicanes (Gaertner et al., 2018). More specifically, 6-hourly SLP fields are used to identify pressure minima after applying a Cressman filter (radius of 200 km; Sinclair, 1997) to smooth out noisy features and small cyclonic structures. Weak cyclones are then filtered with a SLP gradient threshold of 0.5 hPa per 100 km. Cyclone tracks are identified with the aid of the horizontal wind field at 700 hPa, which is considered the steering level for cyclone movement. Then, the CPS is calculated every 6 h based on the track positions and the CPS values at

385   each time step are smoothed using a running mean filter with a 24-h window.

CPS is a descriptor of the three-dimensional thermal structure of cyclones at a given timestep in terms of three parameters: lower-tropospheric horizontal thermal asymmetry (B), which measures the across-track 900-600 hPa thickness gradient, i.e. frontal nature, and thermal winds in the lower ($-V_T^L$; 900-600 hPa) and upper troposphere ($-V_T^U$; 600-300 hPa), which measure the vertical thermal structure. In this three-dimensional parameter space, cyclones can be classified as frontal (B > 0) or

390   non-frontal (B ≤ 0), cold-core ($-V_T^L < 0$; $-V_T^U < 0$), hybrid ($-V_T^L > 0$; $-V_T^U < 0$), or deep warm-core ($-V_T^L > 0$; $-V_T^U > 0$). Cyclones that at least once in their life cycle fulfill the deep warm-core (DWC) criterion are classified as Medicane-like systems.

Based on the results obtained in Sections 6.1 and 6.2, we expect cluster 1 to produce most Medicane-like systems as a strong

Table 1. Number of members with a deep warm-core (DWC) cyclone characteristic in each cluster (bold font).

	cluster 1	cluster 2	cluster 3
# DWC	**15**	**6**	**2**
out of	19	12	18

upper-level PV cut-off is present even after cyclogenesis and there is supply of very moist and warm air in the lower levels.
395 Cluster 3, on the other hand, is expected to produce less Medicane-like systems, as the conditions for the formation of a low-level warm core are much less favorable. Finally, we expect cluster 2 to be placed between clusters 1 and 3, because conditions are favourable for the formation of a low-level warm core but likely the PV cut-off is too weak to maintain cyclonic circulation, destabilization, and forcing for ascent after cyclogenesis.

For each cluster we identify how many members form a DWC cyclone. As shown in Table 1, this is the case for 15 out of
400 the 19 members (79%) in cluster 1. In cluster 3, only 2 out of 18 members (11%) develop a DWC cyclone, and, as expected, cluster 2 shows an intermediate scenario with 6 out of 12 members (50%) producing a DWC cyclone.

Cluster 1 not only produces significantly more DWC cyclones but also shows stronger upper-level warm cores (indicated by the higher $-V_T^U$ values in Fig. 12) and longer duration of the DWC stage (indicated by the number of DWC steps in Fig. 12). Note that, especially for cluster 3, the number of DWC steps has to be considered with caution, due to the small sample size.
405 Nonetheless, these results show that cluster 1 tends to produce not only more but also more robust DWC cyclones. Interestingly, the Medicane in the operational analysis has an upper-level warm core that is on the weaker side of what members in cluster 1 forecasted and is about as strong as the upper-level warm cores produced in clusters 2 and 3. But it maintains a deep warm core about twice as long as the average Medicane in all clusters.

Overall, these findings suggest that cluster 1 provides the best synoptic environment out of the three clusters for a Medicane-
410 like system to form. However, the strength of the upper-level warm core in cluster 1 is overestimated compared to the analysis and the variability among the cluster members is large. This indicates that the synoptic setting in cluster 1 has the potential for much stronger Medicane-like systems than the one that actually occurred. On the contrary, the duration of the deep warm-core stage is strongly underestimated. We conclude that, once the PV streamer is forecasted well, sub synoptic-scale processes including the detailed interaction between the surface cyclone and upper levels become limiting factors to accurately predict the
415 cyclone evolution including its vertical structure.

7 Conclusions

The basis of this study was an ECMWF operational ensemble forecast that showed large uncertainties in the development of Medicane Zorbas in September 2018. The ensemble members were clustered into three distinct scenarios according to the position and shape of a PV streamer over the Mediterranean that lead to the development of Zorbas. The differences between
420 these scenarios were used to provide new insight into, on the one hand, the link between uncertainties in the large-scale flow

and the meso-scale development of the Medicane, and, on the other hand, the origin, amplification and propagation of forecast uncertainties in Rossby waves.

It is clear that the uncertain position of the PV streamer was the dominant factor limiting the predictability of Zorbas for both its location and its vertical thermal structure. The first aspect, the direct influence on the cyclone formation is straightforward,

425 as the PV streamer and cut-off provided the main forcing for cyclogenesis. Regarding the second aspect, the cyclone structure, we identified two possible large-scale key ingredients relevant for the transition of the extratropical cyclone into a sub-tropical cyclone and, consequently, a tropical-like system, i.e. a Medicane. First, low-level advection below the eastern side of the streamer had to be such that dry and cold air masses from Eastern Europe and the Black Sea region were transported rapidly over the Mediterranean. They took up moisture by surface fluxes, experienced diabatic heating and ended up in the cyclone

430 centre, where they helped to form a strong low-level warm core [similar to the first case in Miglietta and Rotunno, 2019)]. The location of cyclogenesis and hence the extent to which this process could be active was directly linked to the position of the PV streamer. Additionally, the PV streamer had to be far enough west for its induced circulation to reach the region with very warm and moist low-level air over the Central Mediterranean and advect it cyclonically around its tip into the warm sector of the cyclone. As a second ingredient, the upper-level PV cut-off had to be strong enough to maintain the cyclonic circulation

435 and destabilize its immediate surrounding to favour deep convection even after cyclogenesis. This is reminiscent of the second Medicane case in Miglietta and Rotunno (2019) and the case discussed in Fita and Flaounas (2018). In most members of cluster 1, both conditions were fulfilled, whereas in cluster 2 the second and in cluster 3 the first condition was mostly missing.

The uncertainties in the position of the PV streamer after 72 h forecast lead time could be clearly linked to relatively large-scale uncertainties in the initial conditions on the stratospheric side of an upper-level jet streak over the Gulf of Saint Lawrence. They

440 propagate along the dynamical tropopause and strongly amplify in the left exit of a jet streak over the North Atlantic. At the same time, the strong QG forcing for ascent in this region enables a coupling of upper and lower levels and initiates a baroclinic wave. This wave and the associated rapid growth, as expected from baroclinic instability, are crucial for the in situ amplification of the uncertainties in this case. Non-linear tropopause dynamics then leads to the rapid downstream development of the uncertainties eventually resulting in the uncertain PV streamer and the development of Zorbas. The contributions of diabatic

445 airstreams, such as warm conveyor belts, were negligible for the uncertainty amplification in this case. The described amplification process could be an important element to better understand the amplification of forecast uncertainties also in other flow situations, especially in the storm track regions. Further case studies as well as more climatological analyses are needed to quantify its relevance.

Since the seminal work of Lorenz (1969), the growth of very small uncertainties on convective scales to large-scale uncer-

450 tainties, so called upscale error growth, has been discussed as theoretical limit of atmospheric predictability (e.g. Zhang et al., 2007). The picture of the flapping wings of a butterfly influencing the development of a storm much later has become well known outside research. However, recent studies suggested that the practical limits of atmospheric predictability often come from uncertainties on much larger scales, even if they are very small compared to the average kinetic energy on that scale (e.g. Durran and Weyn, 2016). This study provides an illustrative example that large-scale, but relative to the background kinetic

455 energy small, uncertainties in an upper-level jet streak over North America can dominate the forecast uncertainty of a storm in

the Mediterranean.

Finally, we note that many other factors may be also relevant for the exact evolution of the Medicane even if the PV streamer is at the right location. The details of the interaction between lower and upper levels, for example, likely influence the formation the warm core, the intensification, and the track of the cyclone. This in turn determines if the cyclone remains over the sea and
460   is able to intensify, or, if it makes landfall and decays. These aspects are subject of a follow-up study.

Data availability. All data is available from the authors upon request

Author contributions. JJGA sparked this work by discovering the uncertain forecast of Zorbas. RP and JJGA designed the basic idea for the study. JJGA carried out the analyses that required the computation of the CPS and RP all remaining analyses. MS and HW helped with the data access and handling and gave important guidance and useful inputs during the whole project. RP and JJGA prepared the manuscript and
465   all authors gave critical feedback that helped to improve the article.

Competing interests. The authors declare that they have no conflict of interest.

Acknowledgements. RP acknowledges funding from the ETH research grant ETH-0716-2. JJGA has been funded through the PhD-grant BES-2014-067905 and grant EEBB-I-18-12841 for short research stays, both by the Spanish Ministry of Science, Innovation and University, and co-funded by the European Social Fund. RP thanks Emmanouil Flaounas (ETH Zurich) for insightful discussions about Medicanes.

470 **References**

Appenzeller C, Davies HC. 1992. Structure of stratospheric intrusions into the troposphere. Nature **358**: 570–572.

Bauer P, Thorpe A, Brunet G. 2015. The quiet revolution of numerical weather prediction. Nature **525**: 47–55.

Baumgart M, Riemer M, Wirth V, Teubler F, Lang STK. 2018. Potential vorticity dynamics of forecast errors: A quantitative case study. Mon. Weather Rev. **146**: 1405–1425.

475 Binder H, Boettcher M, Joos H, Wernli H. 2016. The role of warm conveyor belts for the intensification of extratropical cyclones in Northern Hemisphere winter. J. Atmos. Sci. **73**: 3997–4020.

Cavicchia L, von Storch H, Gualdi S. 2014. A long-term climatology of medicanes. Clim. Dyn. **43**: 1183–1195.

Davies HC, Rossa A. 1998. PV frontogenesis and upper-tropospheric fronts. Mon. Weather Rev. **126**: 1528–1539.

Davies HC, Didone M. 2013. Diagnosis and dynamics of forecast error growth. Mon. Weather Rev. **141**: 2483–2501.

480 Davis CA, Bosart LF. 2004. The TT problem: Forecasting the Tropical Transition of cyclones. Bull. Amer. Meteorol. Soc. **85**: 1657–1662.

Di Muzio E, Riemer M, Fink A, Maier-Gerber M. 2019. Assessing the predictability of Medicanes in ECMWF ensemble forecasts using an object-based approach. Q. J. Royal Meteorol. Soc. **Early View**. https://rmets.onlinelibrary.wiley.com/doi/full/10.1002/qj.3489.

Dirren S, Didone M, Davies HC. 2003. Diagnosis of "forecast-analysis" differences of a weather prediction system. Geophys. Res. Lett. **30**: 2060.

485 Durran DR, Weyn JA. 2016. Thunderstroms do not get butterflies. Bull. Amer. Meteorol. Soc. **97**: 237–243.

ECMWF. 2018. Technical report, https://www.ecmwf.int/en/publications/ifs-documentation. Access date: August 22, 2019

Emanuel KA. 1986. An air-sea interaction theory for tropical cyclones. Part I: Steady-state maintenance. J. Atmos. Sci. **43**: 686–604.

Emanuel KA. 2005. Genesis and maintenance of "Mediterranean hurricanes". Adv. Geosci. **2**: 217–220.

Fehlmann R, Davies HC. 1997. Misforecasts of synoptic systems: Diagnosis via PV retrodiction. Mon. Weather Rev. **125**: 2247–2264.

490 Fita L, Flaounas E. 2018. Medicanes as subtropical cyclones: the December 2005 case from the perspective of surface pressure tendency diagnostics and atmospheric water budget. Q. J. Royal Meteorol. Soc. **144**: 1028–1044.

Gaertner MA, Gonzalez-Aleman JJ, Romera R, Dominguez M, Gil V, Sanchez E, Gallardo C, Marcello Miglietta M, Walsh KJE, Sein DV, Somot S, Dell'Aquila A, Teichmann C, Ahrens B, Buonomo E, Colette A, Bastin S, van Meijgaard E, Nikulin G. 2018. Simulation of medicanes over the Mediterranean Sea in a regional climate model ensemble: impact of ocean-atmosphere coupling and increased
495 resolution. Clim. Dyn. **51**: 1041–1057.

González-Alemán JJ, Valero F, Martín-León F, Evans JL. 2015. Classification and synoptic analysis of subtropical cyclones within the northeastern Atlantic Ocean. J. Clim. **28**: 3331–3352.

González-Alemán JJ, Evans JL, Kowaleski AM. 2018. Use of ensemble forecasts to investigate synoptic influences on the structural evolution and predictability of Hurricane Alex (2016) in the midlatitudes. Mon. Weather Rev. **146**: 3143–3162.

500 Graf MA, Wernli H, Sprenger M. 2017. Objective classification of extratropical cyclogenesis. Q. J. Royal Meteorol. Soc. **143**: 1047–1061.

Grams CM, Magnusson L, Madonna E. 2018. An atmospheric dynamics perspective on the amplification and propagation of forecast error in numerical weather prediction models: A case study. Q. J. Royal Meteorol. Soc. **144**: 2577–2591.

Gray SL, Dunning CM, Methven J, Masato G, Chagnon JM. 2014. Systematic model forecast error in Rossby wave structure. Geophys. Res. Lett. **41**: 2979–2987.

505 Guishard MP, Evans JL, Hart RE. 2009. Atlantic subtropical storms. Part II: Climatology. J. Clim. **22**: 3574–3594.

Guishard MP, Nelson EA, Evans JL, Hart RE, Connell DGO. 2007. Bermuda subtropical storms Meteorol. Atmos. Phys. **253**: 239–253.

Hakim G. 2005. Vertical structure of midlatitude analysis and forecast errors. Mon. Weather Rev. **133**: 567–578.

Hart R. 2003. A cyclone phase space derived from thermal wind and thermal asymmetry. Mon. Weather Rev. **131**: 585–616.

Joos H, Wernli H. 2012. Influence of microphysical processes on the potential vorticity development in a warm conveyor belt: a case-study
510   with the limited-area model COSMO. Q. J. Royal Meteorol. Soc. **138**: 407–418.

Lamberson WS, Torn RD, Bosart LF, Magnusson L. 2016. Diagnosis of the source and evolution of medium-range forecast errors for
       extratropical cyclone Joachim. Weather and Forecasting **31**: 1197–1214.

Leutbecher M, Palmer TN. 2008. Ensemble forecasting. J. Comp. Phys. **227**: 3515–3539.

Lorenz E. 1969. Predictability of a flow which possesses many scales of motion. Tellus **21**: 289–307.

515 Magnusson L. 2017. Diagnostic methods for understanding the origin of forecast errors. Q. J. Royal Meteorol. Soc. **143**: 2129–2142.

Maier-Gerber M, Riemer M, Fink AH, Knippertz P, Di Muzio E, McTaggart-Cowan R. 2019. Tropical Transition of Hurricane Chris (2012)
       over the North Atlantic Ocean: A multiscale investigation of predictability. Mon. Weather Rev. **147**: 951–970.

Martinez-Alvarado O, Madonna E, Gray SL, Joos H. 2016. A route to systematic error in forecasts of Rossby waves. Q. J. Royal Meteorol.
       Soc. **142**: 196–210.

520 Mazza E, Ulbrich U, Klein R. 2017. The Tropical Transition of the October 1996 Medicane in the western Mediterranean sea: A warm
       seclusion event. Mon. Weather Rev. **145**: 2575–2595.

Miglietta MM, Laviola S, Malvaldi A, Conte D, Levizzani V, Price C. 2013. Analysis of tropical-like cyclones over the Mediterranean sea
       through a combined modeling and satellite approach. Geophys. Res. Lett. **40**: 2400–2405.

Miglietta MM. 2019. Mediterranean tropical-like cyclones (Medicanes). Atmosphere **10**: 206.

525 Miglietta MM, Rotunno R. 2019. Development mechanisms for Mediterranean tropical-like cyclones (Medicanes). Q. J. Royal Meteorol.
       Soc. **Early online release**. https://rmets.onlinelibrary.wiley.com/doi/full/10.1002/qj.3503

Pantillon F, Chaboureau JP, Richard E. 2016. Vortex-vortex interaction between Hurricane Nadine (2012) and an Atlantic cut-off dropping
       the predictability over the Mediterranean. Q. J. Royal Meteorol. Soc. **142**: 419–432.

Palmer TN. 2018. The ECMWF ensemble prediction system: Looking back (more than) 25 years and projecting forward 25 years. Q. J. Royal
530   Meteorol. Soc.. 25 Years of Ensemble Forecasting. **Early online release.** https://rmets.onlinelibrary.wiley.com/doi/full/10.1002/qj.3383

Picornell M, Jansa A, Genoves A, Campins J. 2001. Automated database of mesocyclones from the HIRLAM(INM)-0.5 degrees analyses in
       the western Mediterranean. Int. J. Climatol. **21**: 335–354.

Portmann R, Crezee B, Quinting J, Wernli H. 2018. The complex life-cycles of two long-lived potential vorticity cutoffs over Europe. Q. J.
       Royal Meteorol. Soc. **144**: 701–719.

535 Quandt LA, Keller JH, Martius O, Jones SC. 2017. Forecast Variability of the Blocking System over Russia in Summer 2010 and Its Impact
       on Surface Conditions. Weather and Forecasting **32**: 61–82.

Rodwell MJ, Magnusson L, Bauer P, Bechtold P, Bonavita M, Cardinali C, Diamantakis M, Earnshaw P, Garcia-Mendez A, Isaksen L,
       Kaellen E, Klocke D, Lopez P, McNally T, Persson A, Prates F, Wedi N. 2013. Characteristics of occasional poor medium-range weather
       forecasts for Europe. Bull. Amer. Meteorol. Soc. **94**: 1393–1405.

540 Rodwell MJ, Richardson DS, Parsons DB, Wernli H. 2018. Flow-dependent reliability. A path to more skillful ensemble forecasts. Bull.
       Amer. Meteorol. Soc. **99**: 1015–1026.

Schwierz C, Dirren S, Davies H. 2004. Forced waves on a zonally aligned jet stream. J. Atmos. Sci. **61**: 73–87.

Shapiro M, Keyser D. 1990. Fronts, jet streams and the tropopause. In: Extratropical Cyclones: The Erik Palmen Memorial Volume, Newton,
       CW and Holopainen, EO (ed). Amer. Meteorol. Soc. ISBN 1-878220-03-9, pp. 167–191.

545 Sinclair M. 1997. Objective identification of cyclones and their circulation intensity, and climatology. Weather and Forecasting **12**: 595–612.

Sprenger M, Wernli H. 2015. The LAGRANTO Lagrangian analysis tool - version 2.0. Geosci. Model Dev. **8**: 2569–2586.

Torn RD, Whitaker JS, Pegion P, Hamill TM, Hakim GJ. 2015. Diagnosis of the source of GFS medium-range track errors in Hurricane Sandy (2012). Mon. Weather Rev. **143**: 132–152.

Tous M, Romero R. 2013. Meteorological environments associated with medicane development. Int. J. Climatol. **33**: 1–14.

550 Wernli H, Davies HC. 1997. A Lagrangian-based analysis of extratropical cyclones. 1: The method and some applications. Q. J. Royal Meteorol. Soc. **123**: 467–489.

Zhang F, Bei N, Rotunno R, Snyder C, Epifanio CC. 2007. Mesoscale predictability of moist baroclinic waves: Convection-permitting experiments and multistage error growth dynamics. J. Atmos. Sci. **64**: 3579–3594.
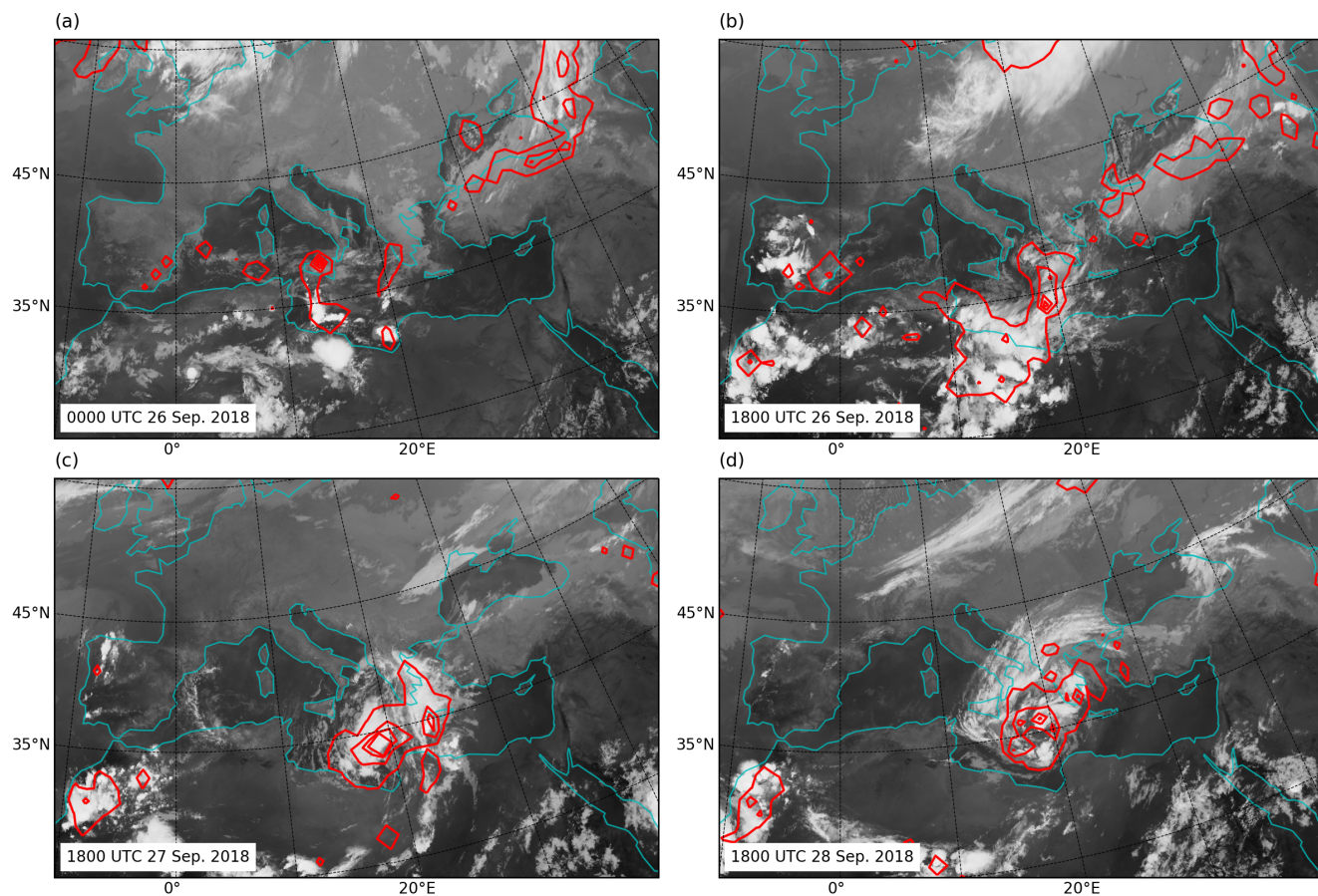
Figure 1. Infrared channel 9 (10.8 μm) of MSG SEVIRI provided by EUMETSAT (grey shading) and total precipitation accumulated over the previous 6 hours based on ECMWF operational short-term forecasts (red contours, 1, 8, 15 and 21 mm (6h)$^{-1}$) at (a) 0000 UTC 26 Sep, (b) 1800 UTC 26 Sep, (c) 1800 UTC 27 Sep, and (d) 1800 UTC 28 Sep 2018.
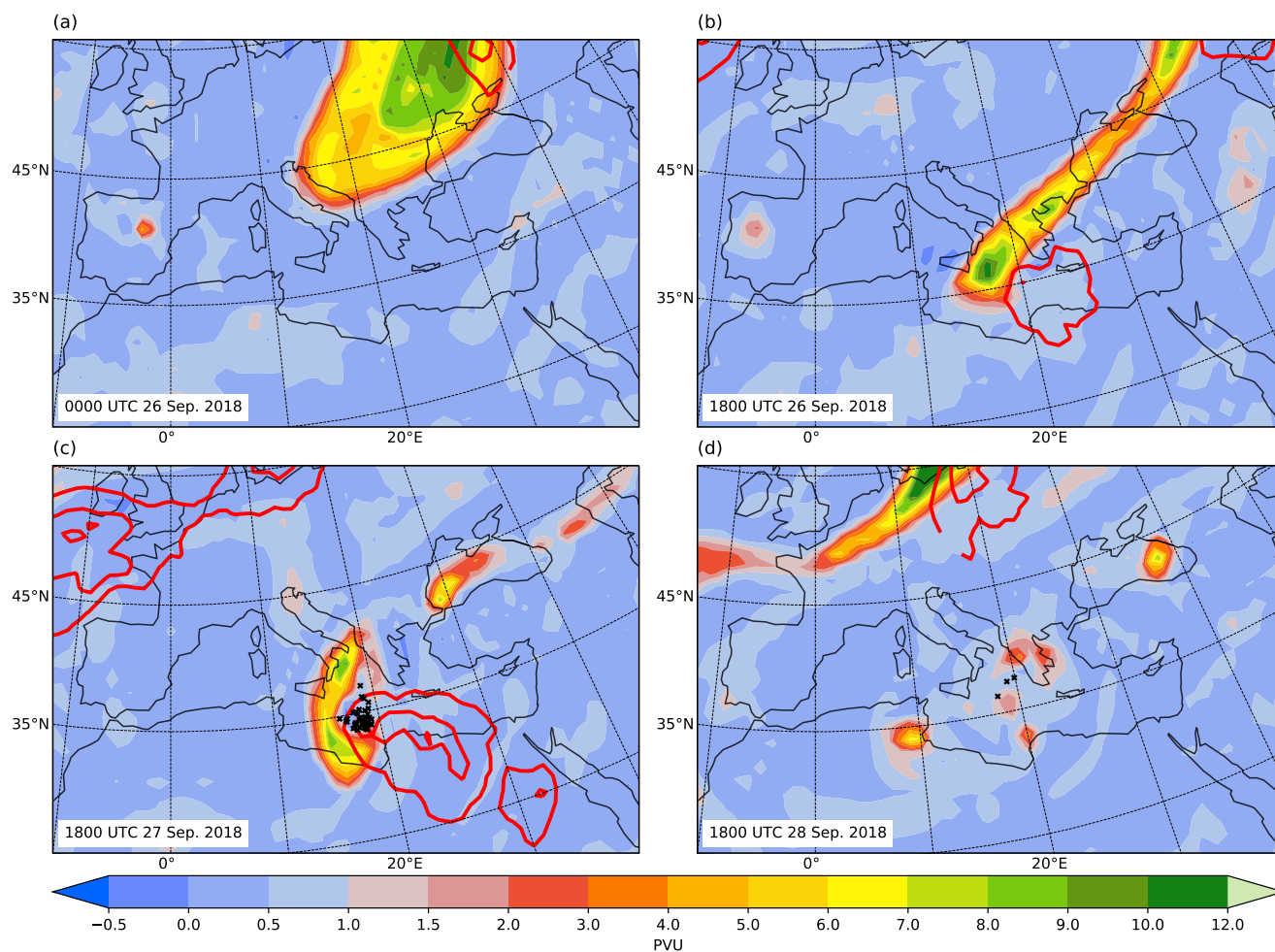
Figure 2. PV on 325 K (shaded, in PVU) and intersection points of air parcels with an ascent rate of more than 600 hPa in 24 h (black crosses), and red contours show QG ω (-0.5 and -1·10^{-2} Pas^{-1}) on 850 hPa as forced from levels above 550 hPa at (a) 0000 UTC 26 Sep, (b) 1800 UTC 26 Sep, (c) 1800 UTC 27 Sep, and (d) 1800 UTC 28 Sep 2018.
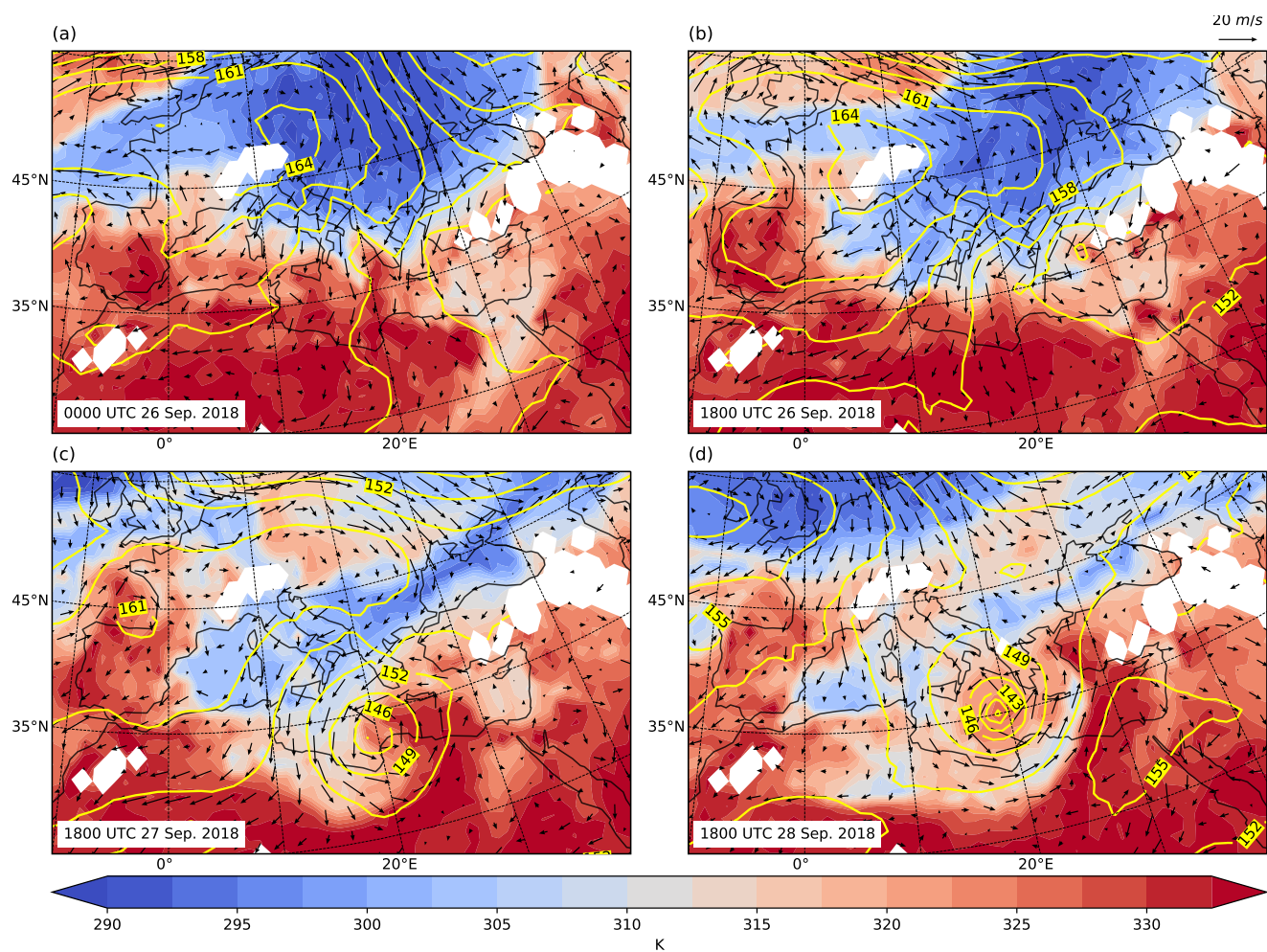
Figure 3. Equivalent potential temperature (shaded, in K), geopotential height (yellow contours, in gpdm) and wind vectors (black arrows) on 850 hPa at (a) 0000 UTC 26 Sep, (b) 1800 UTC 26 Sep, (c) 1800 UTC 27 Sep, and (d) 1800 UTC 28 Sep 2018.
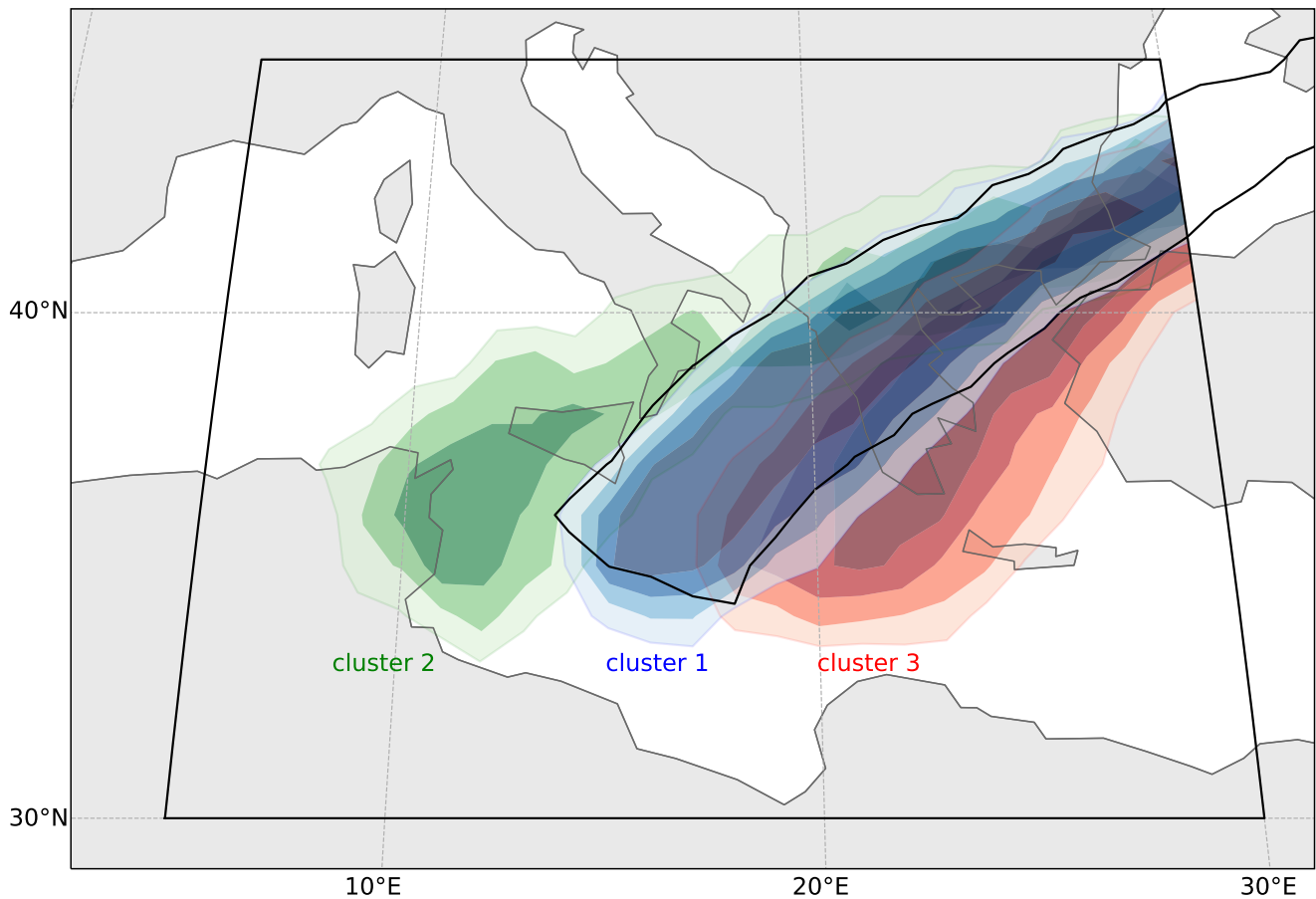
Figure 4. Clustering of ensemble members according to the position of the upper-level PV streamer in the Mediterranean at 0000 UTC 27 Sep 2018. Colors show frequencies of $PV_{av} \geq 2$ PVU (shading, every 20%) for each cluster (blue: cluster 1, green: cluster 2, red: cluster 3) and the black line the $PV_{av} = 2$-PVU contour in the operational analysis. The region considered for the clustering is shown by the black box (see text for details).
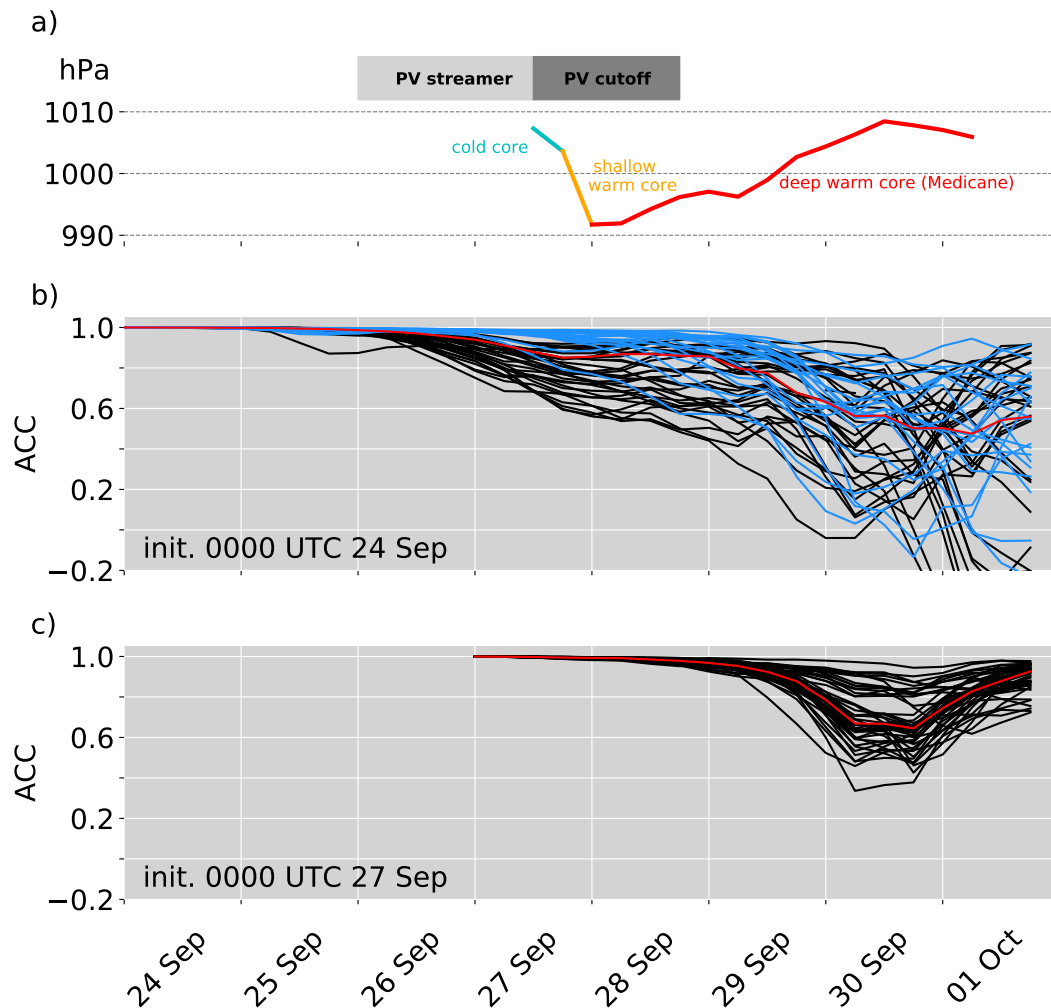
Figure 5. (a) Temporal evolution of synoptic elements discussed in this study. Grey boxes indicate times when the PV streamer or cut-off on 325 K is present in the analysis and the solid line shows the evolution of the minimum sea-level pressure of the cyclone, colors indicate the cyclone stage as identified from the CPS (cold-core: blue, shallow warm-core: orange, deep warm-core: red). (b) and (c) Temporal evolution of the anomaly correlation coefficient of geopotential height at 500 hPa in the Mediterranean box (see Fig. 4) is shown for each ensemble member (black lines, cluster 1: blue lines) and the median (red line) of the ensemble forecast initialized at (b) 0000 UTC 24 Sep 2018 (50 members) and (c) 0000 UTC 27 Sep 2018 (46 members).
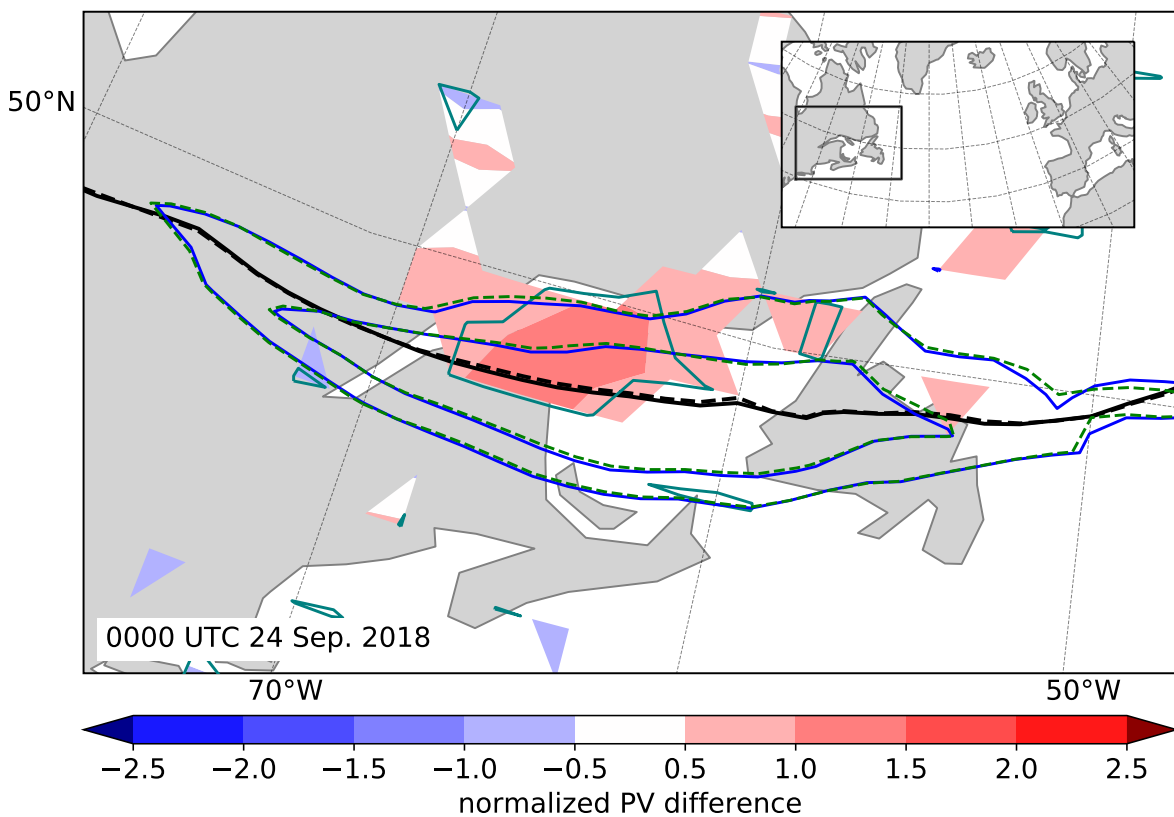
Figure 6. Normalized differences of PV (shaded) between cluster 3 and cluster 2 ($\Delta PV_{3,2}$), regions where they are statistically significant (teal contour), 2-PVU contour (black; cluster 3: solid, cluster 2: dashed) and 60 and 65 ms^{-1} wind speed contours (cluster 3: blue solid, cluster 2: green dashed) on 325 K centered over the Gulf of Saint Lawrence at 0000 UTC 24 Sep 2018, i.e. initialisation time of the ensemble forecast.
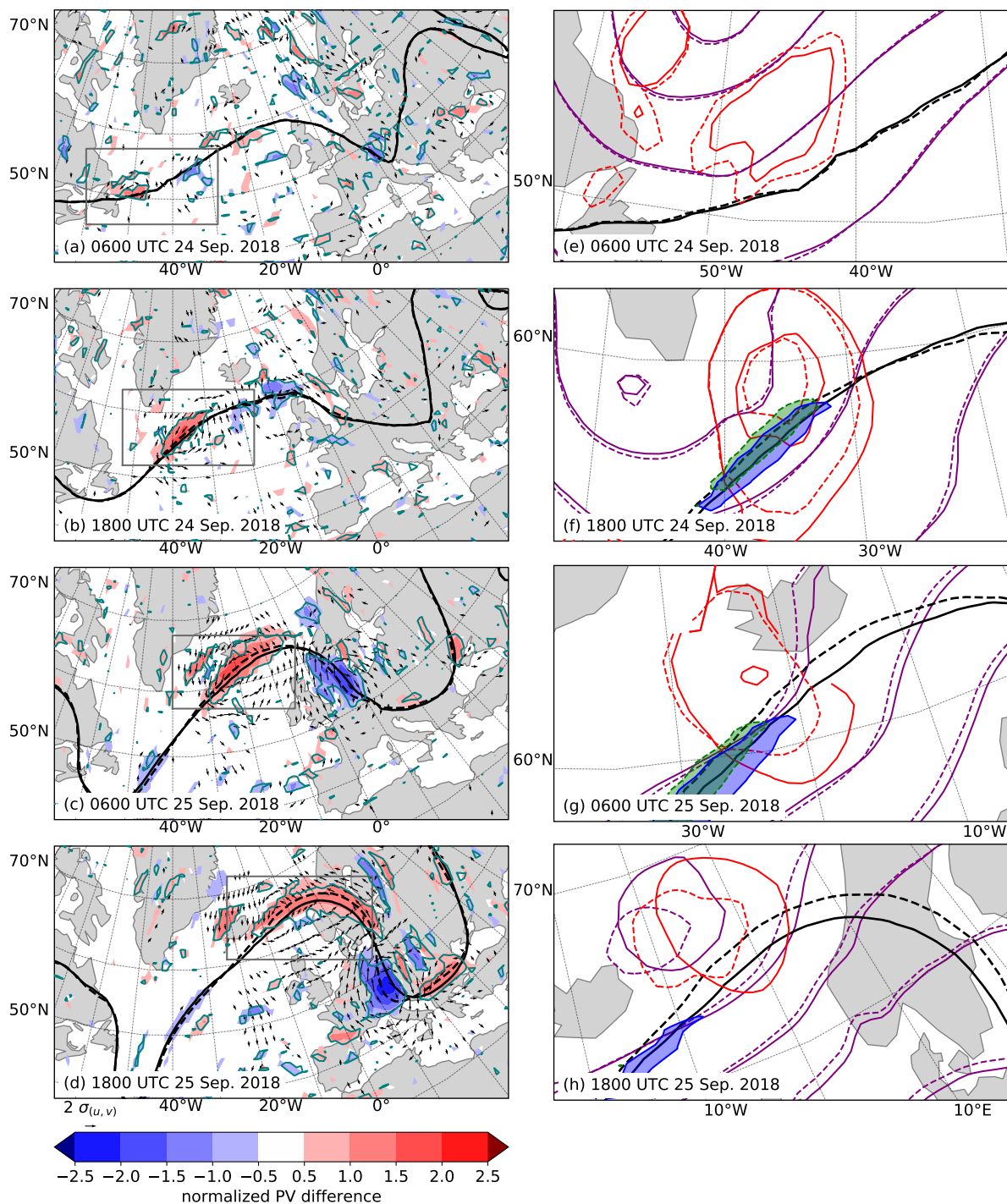
Figure 7. (a-d) Normalized differences of PV (shaded) and winds (arrows, only if larger than 1 standard deviation) on 325 K of cluster 3 and cluster 2 from 0600 UTC 24 Sep 2018 to 1800 UTC 25 Sep 2018 every 12 hours. Regions with statistically significant PV differences (p-value < 0.05) are marked with teal contours. (e-h) For the same timesteps, high wind speeds on 325 K ($>75\,\mathrm{m\,s^{-1}}$, cluster 3: blue, cluster 2: green), QG ω on 850 hPa forced from above 550 hPa (red contours; 0.01,-0.03 and -0.05 $\mathrm{Pa\,s^{-1}}$), geopotential height on 850 hPa (purple contours; every 10 gpdm) for cluster 3 (solid) and cluster 2 (dashed) and 2-PVU contours on 325 K (black contours; cluster 3: solid, cluster 2: dashed).
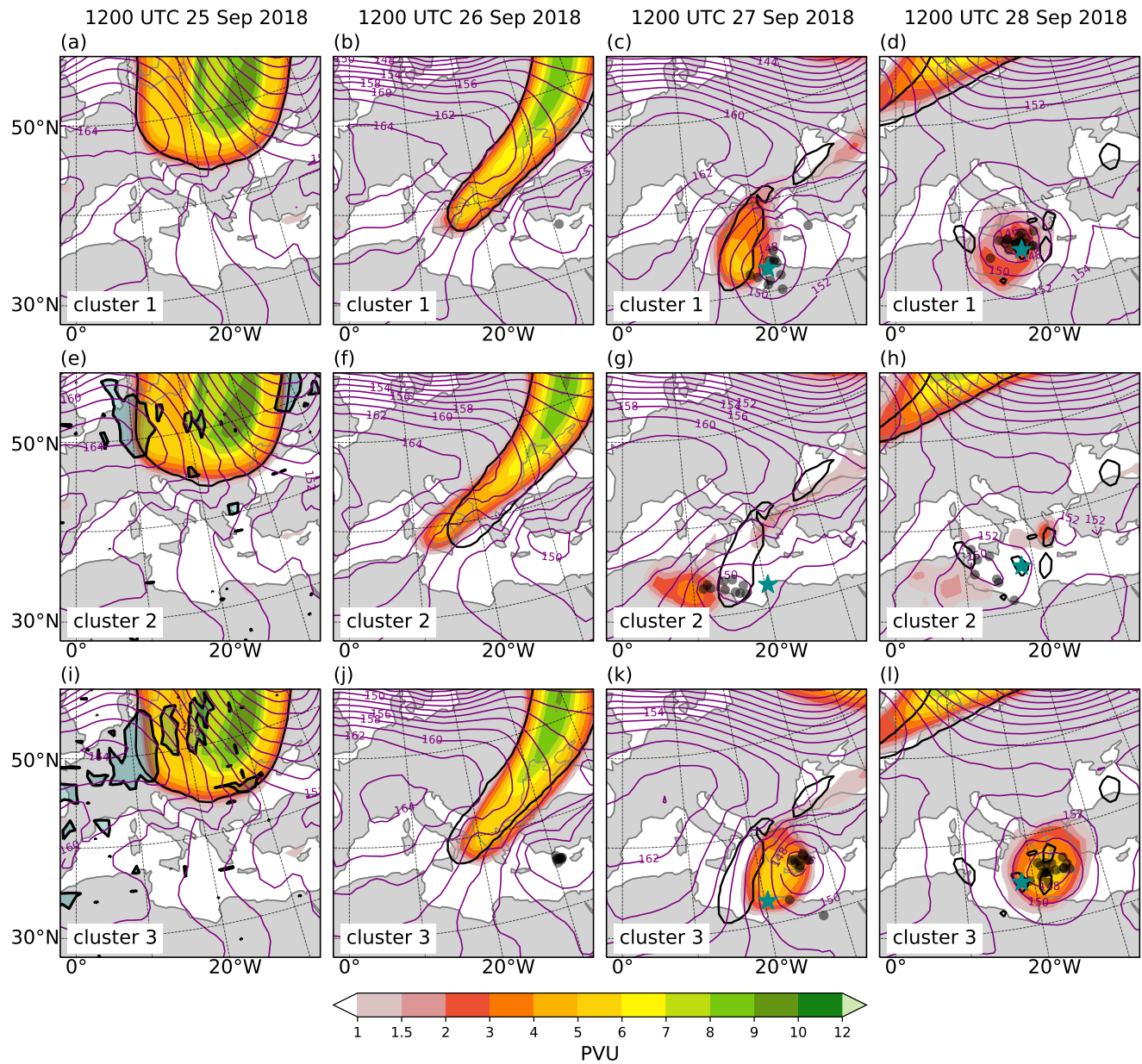
Figure 8. Cluster-mean PV on 325 K (shaded, in PVU), cluster-mean geopotential height on 850 hPa (purple contours, every 2 gpdm), analysis 2-PVU contour on 325 K (black contour), cyclone positions (as identified with the method described in Sect.6.3) in each ensemble member (black dots), and in the operational analysis (teal star) for each cluster from 1200 UTC 25 Sep to 1200 UTC 28 Sep 2018 every 12 h. Additionally, at 1200 UTC 25 Sep 2018 for clusters 2 and 3 regions where the differences to cluster 1 of the PV field on 325 K are statistically significant are shown as teal patches in (e,f) (see supplementary material).
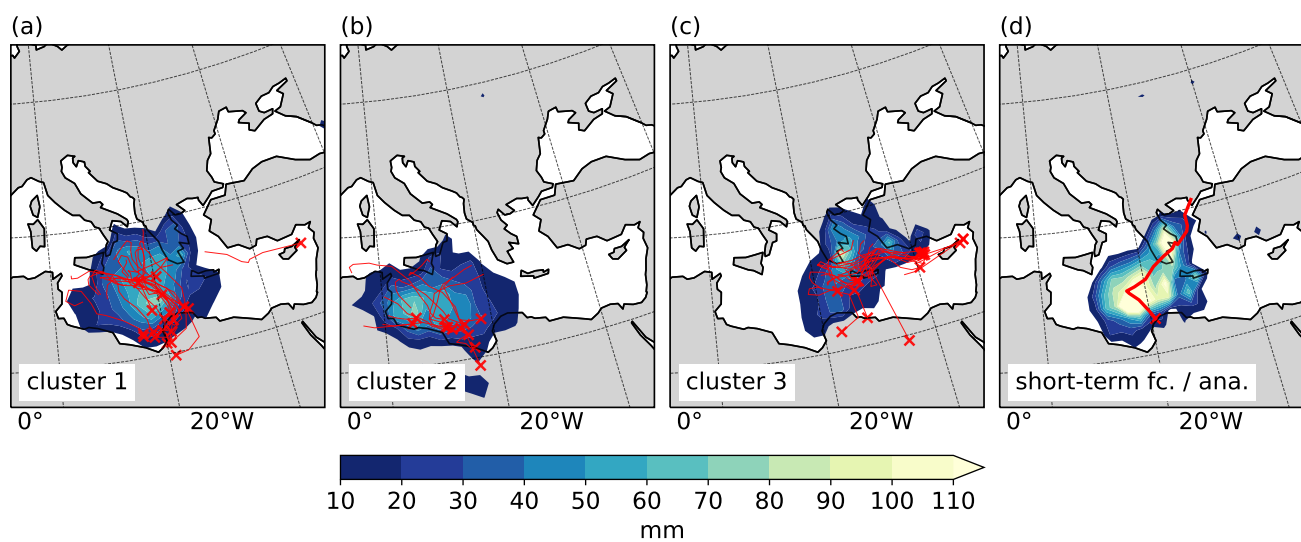
Figure 9. Accumulated precipitation (shading, in mm) from 1800 UTC 26 Sep to 0000 UTC 30 Sep 2018 for (a-c) cluster means of clusters 1-3 and (d) the short-term forecasts. Additionally, red crosses indicate cyclogenesis and red lines cyclone tracks for (a-c) each member and (d) the operational analysis.
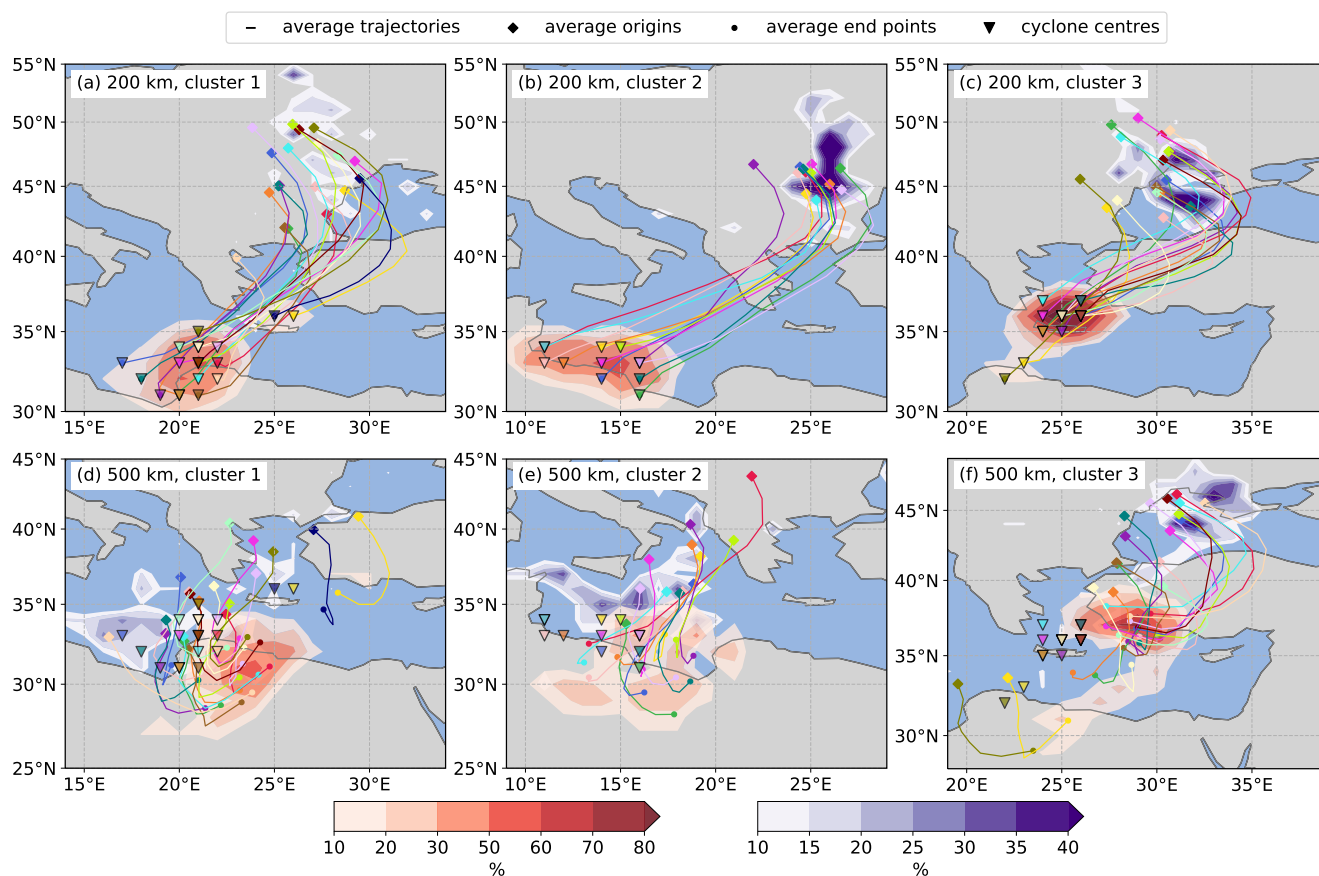
Figure 10. Position of two specific low-level airstreams in the three clusters at 1200 UTC 27 Sep 2018 (red shading) and two days earlier (purple shading). Values (in %) indicate the percentage of ensemble members with an airstream occurring at the specific grid point. The considered airstreams constitute the center of the cyclone on 850 hPa (a-c) and the region with maximum equivalent potential temperature in the cyclone's warm sector on 850 hPa (d-f), see text for details. For each member, the cyclone centres (triangles) as well as average 48-h trajectories of the airstreams for each member (lines) with their origin (diamonds) and end point (dots) are indicated in colors.
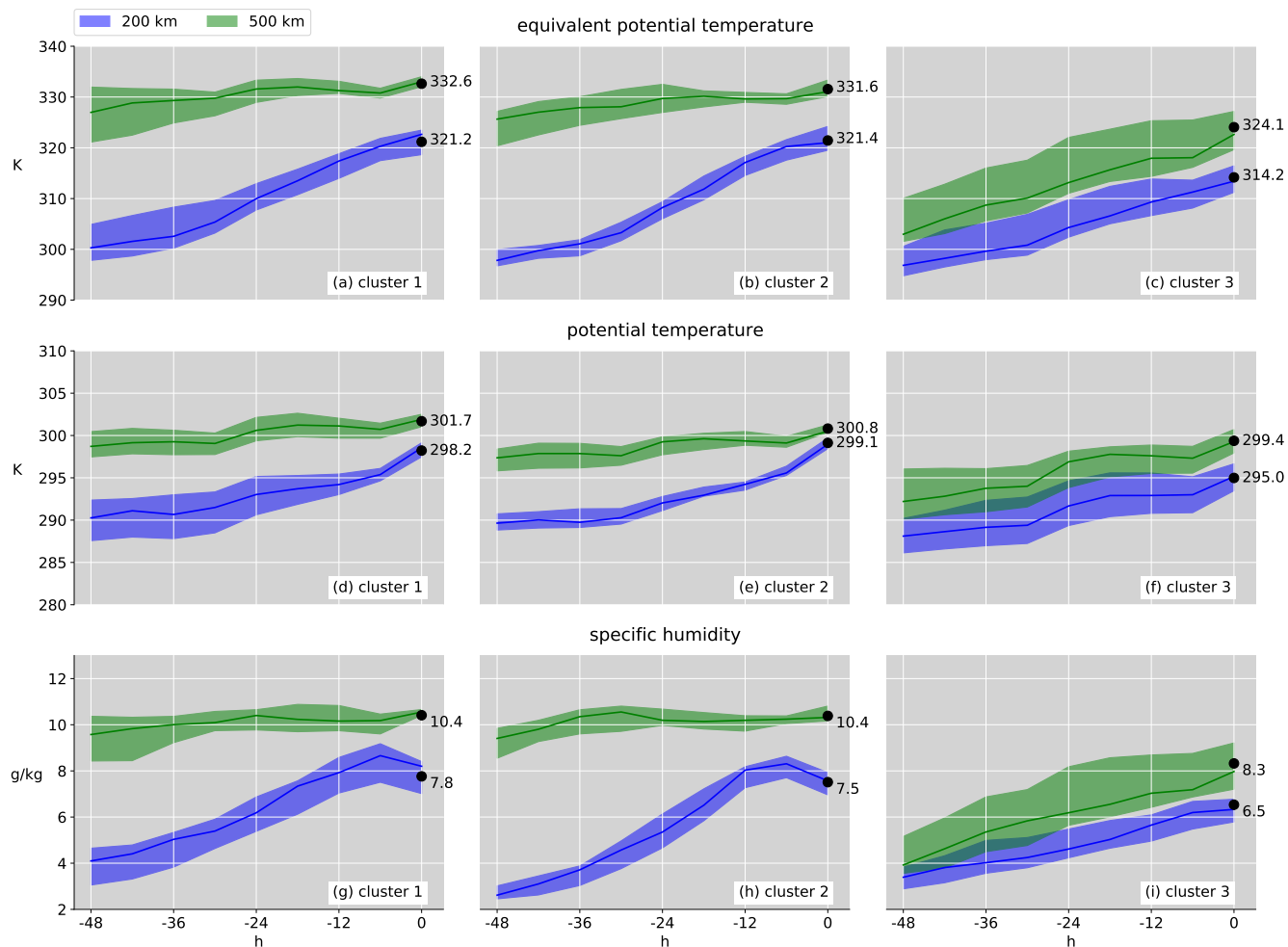
Figure 11. Median (solid line) and the interquartile range (shading) of equivalent potential temperature (a-c), potential temperature (d-f) and specific humidity (g-i) of two specific low-level airstreams, identified as 48-h backward trajectories started at 1200 UTC 27 Sep 2018, from the center of the cyclone on 850 hPa (blue) and the region with maximum equivalent potential temperature in the cyclones warm sectors (green). Values indicate averages of all trajectories of the considered airstreams in each member. Numbers and black dots mark the cluster-average values at 1200 UTC 27 Sep 2018.
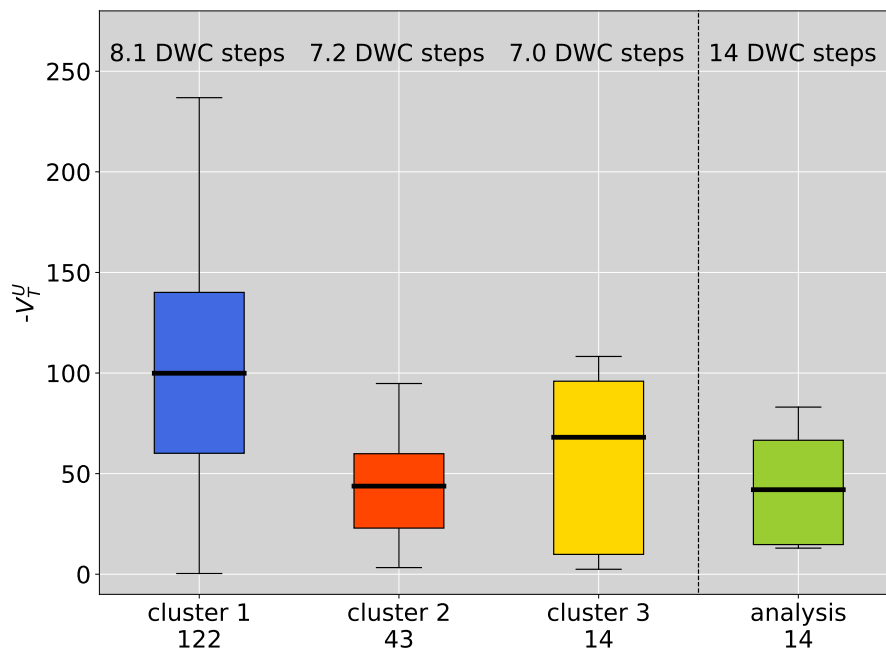
Figure 12. Box plots of all positive $-V_T^U$ values (i.e. time steps with a deep warm core) in all ensemble members, for the three clusters, and in the operational analysis. Numbers on top of each box indicate the average number of deep warm-core (DWC) steps per ensemble member and numbers at the bottom the total number of DWC steps in each box plot.